



## Research Paper

## Free-form surface reconstruction for adaptive imaging with 2D ultrasound arrays



Guillermo Cosarinsky <sup>a</sup>\*, Jorge F. Cruza <sup>a</sup>, Mario Muñoz <sup>a,b</sup>, Adrián Rubio <sup>a,b</sup>, Jorge Camacho <sup>a</sup>

<sup>a</sup> Ultrasound Systems and Technology Group (GSTU), Institute for Physical and Information Technologies (ITEFI), Spanish National Research Council (CSIC), c/Serrano 144, 28006 Madrid, Spain

<sup>b</sup> Electronics Department, Escuela Politécnica, Universidad de Alcalá de Henares, Ctra. Madrid-Barcelona, Km. 33, 600, 28805 Madrid, Spain

## ARTICLE INFO

## Keywords:

Matrix array  
2D array  
3D Imaging  
TFM  
Adaptive imaging  
Autofocusing  
Ultrasound Imaging  
robotic scanning

## ABSTRACT

This paper introduces the Aperture Interpolation Method (AIM) for free-form surface reconstruction using 2D ultrasound arrays. Surface reconstruction plays an essential role in adaptive imaging methods, allowing for effective operation even with imprecise or unknown system geometries. The AIM method leverages the time of flight (TOF) of echos from surface reflections to estimate the surface geometry of a component under test, without requiring a pre-existing component model. In this paper we present the theoretical basis of AIM for three acquisition modes: pulse-echo, pitch-catch, and plane wave. Experimental validation is performed using a complex-shaped aluminum test piece scanned with an 11x11, 3MHz matrix array mounted on a robotic arm. The ultrasonically reconstructed surface is compared with laser scanning data for accuracy analysis. Furthermore, the ultrasonically measured surface data is used to generate Total Focusing Method (TFM) images of the component, which are then compared against micro-CT images for validation. The experimental results validate the AIM method's capability to accurately reconstruct surfaces, facilitating reliable imaging of the components defects, thereby demonstrating its potential applicability in industrial settings.

## 1. Introduction

Ultrasonic non-destructive testing (NDT) is a prevalent technique for the inspection of industrial and structural components. Proper coupling between the ultrasound transducer and the component under test is essential for ultrasound testing (UT), facilitating the efficient transfer of acoustic energy necessary for inspection. Immersion testing is a widely used NDT coupling technique when rigid wedges are unsuitable, such as with curved components or where consistent contact is mechanically challenging. The presence of a coupling medium between the transducer and component under test leads to wave refraction at the component's surface. This complicates the calculation of ray paths for inspection, because the two-point ray tracing [1] need to compute the time of flight (TOF) between a source and a point inside the component requires using iterative search algorithms. Furthermore, the surface shape must be known, which in the case of a rigid wedge is known by design, but in immersion testing must be usually measured, as in the case of complex components with varying curvature [2].

Ultrasound testing using array probes composed of many transducer elements (Fig. 1) is increasingly popular due to their superior flexibility compared to single-element probes [3]. Specifically, an array

transducer can generate an entire ultrasound image from a single transducer position. The most common imaging method is Phased Array (PA), where the ultrasound beam is steered and focused electronically through delay control of individual array elements [4]. The set of delays needed to generate a specific beam pattern is known as a focal law. To determine these focal laws, the time of flight (TOF) between each array element and each desired focal point must be calculated. Therefore, when imaging through a coupling medium, surface shape and element location should be known for ray-tracing. This geometrical information can be estimated by analyzing the echoes created by reflection of the ultrasonic waves at the surface. Many researchers have explored solutions to this problem, employing various signal acquisition and processing techniques. These techniques fall into two major categories: the first one focuses on extracting the surface echo TOF  $t_S(i)$  captured by the  $i$ th array element to calculate surface points. This approach is seen in [2,5–7], where pulse-echo and pitch-catch acquisition methods are used. In [8], a method using plane wave acquisition is also proposed.

The second category relies on imaging. It uses Full Matrix Capture (FMC) and the Total Focusing Method (TFM) [9] to generate an image

\* Corresponding author.

E-mail address: [g.cosarinsky@csic.es](mailto:g.cosarinsky@csic.es) (G. Cosarinsky).

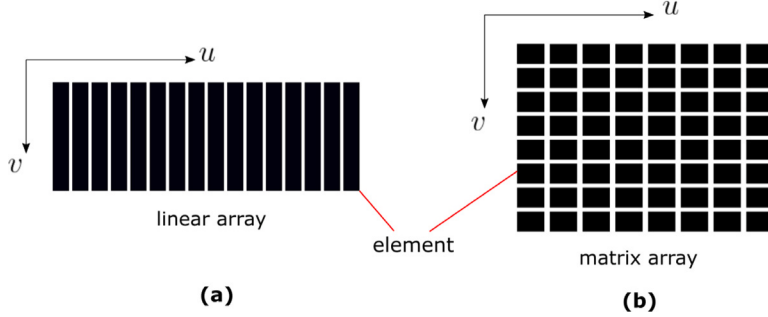


Fig. 1. Schematic of array probes. (a) Linear array, (b) 2D array.

of the first propagation medium. The component surface shows up as a thin bright region in this image, which is used to reconstruct its shape. In [2] both types (TOF and TFM based) of algorithms were developed, concluding that TFM, though more accurate, is slower than TOF methods, because it analyzes full signals rather than a set of TOFs, which comprises a smaller dataset (only one number per signal). In [6] the authors introduce a different image-based algorithm that avoids full image creation, reducing computational load. They also proposed a TOF based method. After comparing their algorithms to the ones proposed in [8], they determined that while all methods yielded similar accuracy, the pitch-catch method resulted in the least execution time.

The methods presented in the previously cited works apply to linear arrays (Fig. 1.(a)), which are the most common type. However, they suffer from some limitations. Linear arrays rely on an image plane that must stay perpendicular to the tested component. This ensures the beam stays within that plane. Misalignment or complex component shapes break this perpendicularity, causing rays to refract outside the image plane potentially harming image quality. Unlike linear arrays, which require strict perpendicularity to the component, 2D arrays offer volumetric beam steering, mitigating the impact of minor angular deviations. This capability allows for imaging beyond a single plane. Moreover, as 2D array elements are small in both lateral dimensions, they exhibit enhanced angular sensitivity compared to linear arrays in their passive direction. This allows capturing rays deflected on the component surface in all spatial directions. This flexibility makes 2D arrays particularly well-suited for complex testing scenarios. Despite their potential, surface reconstruction using 2D arrays remains a relatively unexplored area of research. Within the few works on the subject, [10] presents a TFM-based method, and a TOF-based pulse-echo method was proposed by our group in [11]. We have recently presented in [12] another TOF based method aimed to some elementary shaped components (planes, cylinders and spheres), in which the probe location and orientation (PLO) relative to the component is estimated by fitting a model to the measured TOFs. This method offers a contrasting view to the methodologies in all the cited works, where there is no model assumed, and surface points are locally computed. While this model free approach is more general, a model fitting approach provides a global geometry estimation.

In this article a new TOF based model free approach is presented, which we call Aperture Interpolation Method (AIM). In TOF based methods the differences in  $t_S(i)$  between neighboring array elements gives information of the normal vector to the surface at the reflection point. For these methods to work properly, the measured times of arrival  $t_S^*(i)$  need some type of smoothing filter, as spline or polynomial fitting, which results in a continuous function  $t_S(u)$  where  $u$  is the element coordinate along the array. Unlike methods presented in [2, 5–8], which use finite differences, in the AIM method we leverage the continuous function  $t_S(u)$  to use derivatives to construct a continuous mapping from points in the probe aperture to points on the surface  $S$ . In the case of a 2D array, the fitting (interpolation) of the measured times of flight results in a two variable function  $t_S(u, v)$ , where  $(u, v)$  are the coordinates of the array elements. This function is the object used in the

AIM method to compute the reflecting surface  $S$ . As the array elements can be considered as a spatial sampling of the transducer aperture, the function  $t_S(u, v)$  is the result of interpolating the sampled aperture, thus the name given to the method.

This article first presents the theoretical basis of the proposed method (Section 2). It then demonstrates experimental validation using a test component, comparing ultrasonic results with laser scanning for accuracy analysis (Sections 3 and 4). Finally, the ultrasonically measured surface data is used to generate Total Focusing Method (TFM) images of the component, which contains artificial defects. These images are compared against microCT images for further validation.

## 2. Aperture Interpolation Method (AIM)

In this section we derive the equations of the AIM method for three types of acquisition modes: pulse-echo, pitch-catch and plane wave. The testing configuration is shown in Fig. 2. We consider two coordinate systems: the Probe Coordinate System (PCS), with axes  $(u, v, w)$  and origin  $O_p$ , and the World Coordinate System (WCS) with axes  $(x, y, z)$  and origin  $O_w$ . The PCS is fixed to the probe, and the aperture lays onto the  $uv$  plane. Thus, an array element  $E$  has PCS coordinates  $(u, v, 0)$ , and its position vector is  $\vec{e} = u\hat{u} + v\hat{v}$ . On the other hand, the WCS is fixed to the component under test. We use  $E$  to denote both an array element and its center point, and  $G$  to denote points on the component surface  $S$ . The surface is considered smooth at the operating wavelength, leading to predominantly specular reflection.

### 2.1. AIM with pulse-echo acquisition

For the derivation of this method we use de PCS. To denote the position vector of an element  $E$  we use  $\vec{e} = \overline{O_p E}$  and for the reflection point  $\vec{g} = \overline{O_p G}$ . Fig. 3 illustrates the geometrical relations needed to find, for a given aperture point  $\vec{e}$ , the corresponding surface point  $\vec{g}(\vec{e})$ . The one-way distance traveled by the ray is  $D(\vec{e}) = \|\vec{E}\vec{G}\| = \frac{c_1}{2} t_S(\vec{e})$ , where  $c_1$  is the wave propagation speed in the immersion medium. For two neighboring aperture points, the corresponding rays can be thought as reflecting on the surface tangent plane at  $G$  (Fig. 3.a). Defining  $\vec{v}(\vec{e}) = \vec{g}(\vec{e}) - \vec{e}$ , from Fig. 3.b we know that  $D(\vec{e}) = \|\vec{v}(\vec{e})\|$  and the following relation holds:

$$D(\vec{e} + \vec{d}e) - D(\vec{e}) = \vec{d}e \cdot \hat{n} \quad (1)$$

where  $\vec{d}e$  is the vector between two neighboring elements, and  $\hat{n}$  is the surface normal at  $\vec{e}$ .

Using the first order approximation:

$$D(\vec{e} + \vec{d}e) - D(\vec{e}) = \vec{\nabla}D \cdot \vec{d}e \quad (2)$$

Combining Eqs. (1) and (2) and using the surface normal vector PCS coordinates  $[\hat{n}]_p = (n_u, n_v, n_w)$  we get:

$$\frac{\partial D}{\partial u} du + \frac{\partial D}{\partial v} dv = n_u du + n_v dv \quad (3)$$

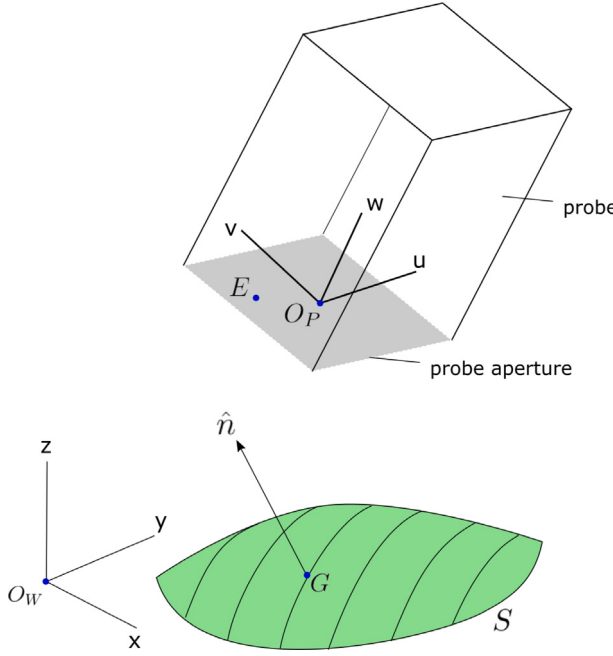


Fig. 2. Schematic of the immersion testing configuration.

As (3) holds for every  $(du, dv)$ , then:

$$\begin{aligned} n_u &= \frac{\partial D}{\partial u} \\ n_v &= \frac{\partial D}{\partial v} \end{aligned} \quad (4)$$

The third component of  $\hat{n}$  can be found by the norm condition  $\|\hat{n}\| = 1$ :

$$n_w = \pm \sqrt{1 - n_u^2 - n_v^2} \quad (5)$$

where + is chosen for an upward normal pointing to the first medium. The normal vector, combining Eqs. (4) and (5), can be expressed as:

$$\hat{n} = \vec{\nabla} D + \hat{w} \sqrt{1 - \vec{\nabla} D \cdot \vec{\nabla} D} \quad (6)$$

where  $\hat{w}$  is the PCS basis vector in  $w$  direction (Fig. 3). As the vector  $\vec{v}(\vec{e})$  is parallel to  $\hat{n}$ , we get the mapping:

$$\vec{g}(\vec{e}) = \vec{e} - D(\vec{e})\hat{n} \quad (7)$$

which maps the array aperture to a surface patch. This mapping is equivalent to the Inverse Boundary Scattering Transform (IBST) derived in [13,14] for pulse radar systems.

## 2.2. AIM with pitch-catch acquisition

Fig. 4 illustrates the geometry of the pitch-catch case, in which there is one emitter  $E_{tx}$  and all the array elements receive the echoes generated by the surface. The ray received by an element  $E$  is reflected on  $G$ , and for elements close to  $E$ , the received rays can be thought as reflecting on the surface tangent plane at  $G$  where the surface normal is  $\hat{n}$  (Fig. 4.a). In this case we define  $D(\vec{e}) = c_1 t_S(\vec{e})$  as the two way length traveled by the ray from  $E_{tx}$  to  $E$ . The  $D(\vec{e})$  of rays received by  $E$  and its neighboring elements can be computed using  $E_{tx}$  mirror image by the tangent plane. This point is called  $E_{tx}^*$  and is shown in Fig. 4.b. Defining vector  $\vec{q} = \overline{E_{tx} E_{tx}^*}$ , in a small region around  $E$  we can approximate  $D(\vec{e})$  as:

$$D(\vec{e}) = \|\vec{e} - \vec{q}\| = \sqrt{(u - q_u)^2 + (v - q_v)^2 + q_z^2} \quad (8)$$

If we can find point  $E_{tx}^*$  we can then find the tangent plane at  $G$ , as it is the plane orthogonal to  $\vec{q}$  and equidistant from  $E_{tx}$  and  $E_{tx}^*$ . The surface point  $G$  can be found as the intersection of the tangent plane with the line from  $E$  to  $E_{tx}^*$ .

The problem we need to solve is how to find  $E_{tx}^*$  knowing  $D(\vec{e})$ , which is the quantity measured from the TOF (as we suppose  $c_1$  known). With the aid of Eq. (8) we can compute  $D^2$  partial derivatives:

$$\begin{aligned} \frac{\partial D^2}{\partial u} &= 2D \frac{\partial D}{\partial u} = 2(u - q_u) \\ \frac{\partial D^2}{\partial v} &= 2D \frac{\partial D}{\partial v} = 2(v - q_v) \end{aligned} \quad (9)$$

From Eq. (9) we can solve for  $(q_u, q_v)$ :

$$\begin{aligned} q_u &= u - D \frac{\partial D}{\partial u} \\ q_v &= v - D \frac{\partial D}{\partial v} \end{aligned} \quad (10)$$

The third component  $q_z$  is found using Eq. (8):

$$q_z = \pm \sqrt{D^2 - \left(u - D \frac{\partial D}{\partial u}\right)^2 - \left(v - D \frac{\partial D}{\partial v}\right)^2} \quad (11)$$

Thus, recalling that  $\vec{e} = u\hat{u} + v\hat{v}$ , vector  $\vec{q}$  can be expressed as:

$$\vec{q} = \vec{e} - \vec{\nabla} D^2 - \hat{w} \sqrt{D^2 - (\vec{e} - \vec{\nabla} D^2) \cdot (\vec{e} - \vec{\nabla} D^2)} \quad (12)$$

where we used the - sign in Eq. (11) because  $\vec{q}$  must be below the  $u$ - $v$  plane.

It is important to note that although we are dealing with vectors in 3D space, as we are supposing a planar probe, the array element position vector  $\vec{e}$  is confined to the  $(u, v)$  plane,  $D$  is a two variable function, and its gradient is also confined to that plane.

In order to find  $G$ , we observe in Fig. 4.b that any point in the tangent plane, whose position vector we call  $\vec{r}$ , satisfies:

$$\left(\vec{r} - \frac{1}{2}\vec{q}\right) \cdot \vec{q} = 0 \quad (13)$$

Point  $G$  is the intersection of the tangent plane with the line from  $E$  to  $E_{tx}^*$ . This line can be parameterized as:

$$\vec{r}(\alpha) = \alpha(\vec{e} - \vec{q}) + \vec{q} \quad (14)$$

Inserting Eq. (13) into (14) we get:

$$\alpha = \frac{\vec{q} \cdot \vec{q}}{2(\vec{q} - \vec{e}) \cdot \vec{q}} \quad (15)$$

Finally, the obtained mapping from  $\vec{e}$  to  $\vec{g}$  is:

$$\vec{g}(\vec{e}) = \frac{\vec{q} \cdot \vec{q}}{2(\vec{q} - \vec{e}) \cdot \vec{q}}(\vec{e} - \vec{q}) + \vec{q} \quad (16)$$

## 2.3. AIM with plane wave acquisition

In this case a plane wave is emitted with a direction given by the unit vector  $\hat{k}$  and all elements receive the echoes. The plane wave is emitted using a focal law such that at  $t = 0$  (the time at which acquisition starts) the wave front goes through the aperture center  $O_P$  (coordinate origin of PCS). Fig. 5 illustrates the geometrical relations involved. For a surface point  $G$  the plane wave locally reflected ray has a direction  $\hat{k}^*$  which is the mirror image of  $\hat{k}$  produced by the tangent plane at  $G$  (Fig. 5). In a small neighborhood of  $G$  the incident wave can be approximated as reflecting on the tangent plane. Thus, we can locally approximate the reflected wave as a plane wave with direction  $\hat{k}^*$  which at  $t = 0$  goes through  $O_P^*$ , the mirror image of  $O_P$  (Fig. 5). The distance traveled by the reflected plane wave to element  $E$  is given by:

$$D(\vec{e}) = \hat{k}^* \cdot (\vec{e} - \vec{p}^*) \quad (17)$$

where  $\vec{p}^*$  is  $O_P^*$  position vector and the reflected wave direction vector  $\hat{k}^*$  is:

$$\hat{k}^* = \hat{k} - 2(\hat{k} \cdot \hat{n})\hat{n} \quad (18)$$

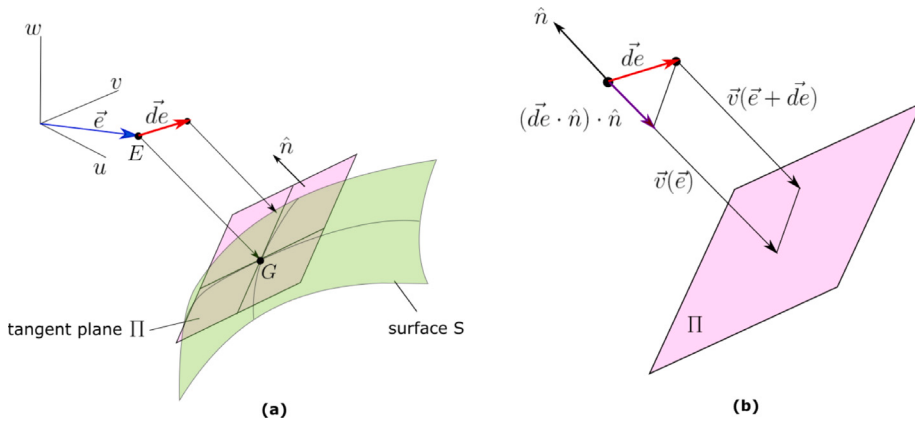


**Fig. 3.** Schematic for the derivation of AIM in pulse-echo mode. (a) Surface and tangent plane with some of the vectors involved in the calculations, (b) Tangent plane and detailed diagram of vector relations.

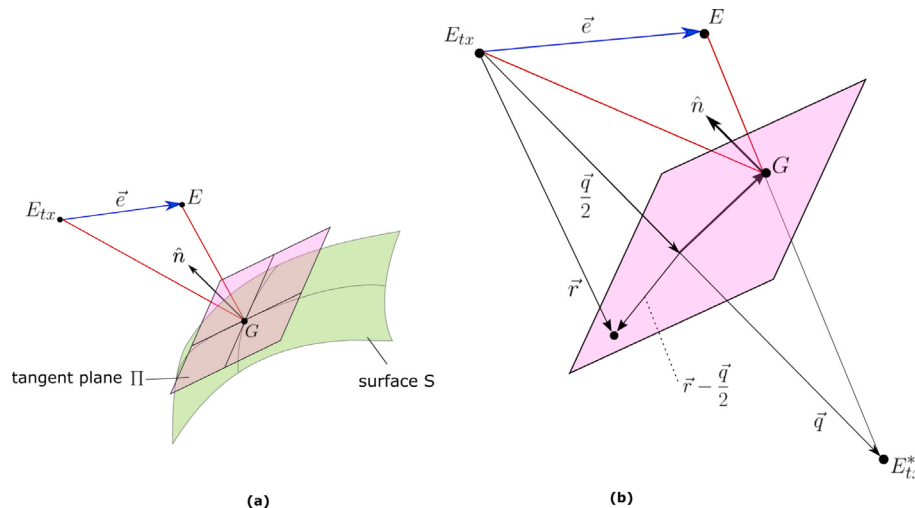


**Fig. 4.** Schematic for the derivation of AIM in pitch-catch mode. (a) Surface and tangent plane with some of the vectors involved in the calculations, (b) Tangent plane and detailed diagram of vector relations.

In order to find the surface normal we use (17) to compute the differential  $dD$ , we use the first order approximation (Eq. (2)):

$$dD = D(\vec{e} + \vec{de}) - D(\vec{e}) = \hat{k}^* \cdot \vec{de} \quad (19)$$

To simplify notation let us define the variable  $\zeta$ :

$$\zeta = \hat{k} \cdot \hat{n} = k_u n_u + k_v n_v + k_w n_w \quad (20)$$

Then, using Eq. (18) and the first order approximation, Eq. (19) becomes:

$$\frac{\partial D}{\partial u} du + \frac{\partial D}{\partial v} dv = (k_u - 2\zeta n_u)du + (k_v - 2\zeta n_v)dv \quad (21)$$

As was done with Eq. (3), we get from (21) the partial derivatives:

$$\frac{\partial D}{\partial u} = (k_u - 2\zeta n_u) \quad (22)$$

$$\frac{\partial D}{\partial v} = (k_v - 2\zeta n_v)$$

we have now 2 equations but 3 unknowns (the normal vector coordinates). The third necessary equation is the unit norm condition:

$$n_u^2 + n_v^2 + n_w^2 = 1 \quad (23)$$

Eqs. (22) and (23) conform a system of three quadratic equations we need to solve for  $(n_u, n_v, n_w)$ . To simplify the algebra we will analyze the case in which  $k_v = 0$ . The general case can be reduced to this case by using a new coordinate system PCS', which is the rotation of PCS around its  $w$  axis by an angle  $\phi = \arctan(\frac{k_v}{k_u})$ .

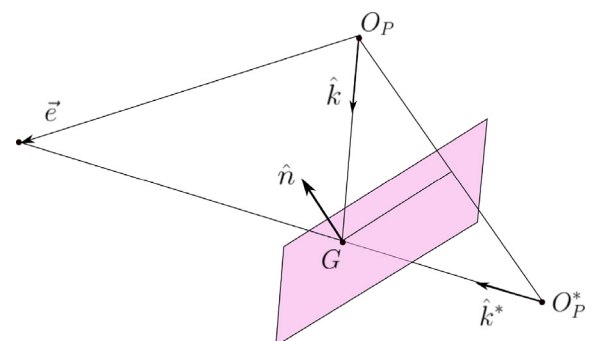


**Fig. 5.** Schematic for the derivation of AIM in plane wave mode.

From Eq. (22) using  $k_v = 0$  we can define a parameter  $\gamma$  that does not depend on the unknowns:

$$\gamma = \frac{n_v}{n_u} = \frac{\frac{\partial D}{\partial v}}{\frac{\partial D}{\partial u} - k_u} \quad (24)$$

Using (24) in (23):

$$n_w = (1 - n_u^2(1 + \gamma^2))^{1/2} \quad (25)$$

where we have chosen the positive square root in order to use a surface normal pointing towards the first propagation medium (as drawn in Fig. 5)

$$\frac{1}{2} \left( \frac{\partial D}{\partial u} - k_u \right) = n_u \left( k_u n_u + k_w (1 - n_u^2(1 + \gamma^2))^{1/2} \right) \quad (26)$$

Eq. (26) can be solved for  $n_u$ , but in the general case it should be solved numerically for each  $D$  and  $\hat{k}$ . Nevertheless there is a special case where an analytical solution is possible: when  $k_u = 0$ . This corresponds to a plane wave parallel to the probe face. It is an important case because if there is no information about the surface orientation this is the most neutral choice for wave direction, and the one for which the angular sensitivity is maximum. The wave direction vector in this case is  $(k_u, k_v, k_w) = (0, 0, -1)$ , thus (26) can be rewritten as second degree equation with  $n_u^2$  as unknown:

$$(1 + \gamma^2)(n_u^2)^2 - n_u^2 - \left( \frac{1}{2} \frac{\partial D}{\partial u} \right)^2 = 0 \quad (27)$$

After some algebraic manipulation the roots of (27) can be expressed as:

$$n_u^2 = (2(1 + \gamma^2))^{-1} \left( 1 \pm \sqrt{1 - \vec{\nabla}D \cdot \vec{\nabla}D} \right) \quad (28)$$

There are four solutions for  $n_u$ . To choose the right one, we use (25) and (28) to get  $n_w$ :

$$n_w^2 = \frac{1}{2} \left( 1 \pm \sqrt{1 - \vec{\nabla}D \cdot \vec{\nabla}D} \right) \quad (29)$$

There is a physical constrain for  $n_w$ . If the absolute value of the angle between  $\hat{n}$  and the  $w$ -axis were larger than  $45^\circ$ , the reflected ray would travel downwards and never reach the probe aperture. Thus the constrain is  $n_w^2 > \cos(45^\circ) = \frac{1}{2}$ . Because of this constrain we must choose the + sign in Eq. (28). Additionally for the surface to point towards the first medium,  $n_w$  should be positive, which finally results in:

$$n_w = \frac{1}{2} \left( 1 + \sqrt{1 - \vec{\nabla}D \cdot \vec{\nabla}D} \right) \quad (30)$$

The other two components of the surface normal can now be computed using (22) as:

$$\begin{aligned} n_u &= \frac{1}{2} \frac{\partial D}{\partial u} n_w^{-1} \\ n_v &= \frac{1}{2} \frac{\partial D}{\partial v} n_w^{-1} \end{aligned} \quad (31)$$

Once known the surface normal we can compute the corresponding surface point vector  $\vec{g}$  by the following reasoning. From Fig. 5 we observe that:

$$\vec{p}^* = 2(\vec{g} \cdot \hat{n})\hat{n} \quad (32)$$

Using (17), (18) and (32) the following relation is found:

$$D = (\vec{e} - 2(\vec{g} \cdot \hat{n})\hat{n}) \cdot (\hat{k} - 2(\hat{k} \cdot \hat{n})\hat{n}) = 2\zeta(\vec{e} - \vec{g}) \cdot \hat{n} + \vec{e} \cdot \hat{k} \quad (33)$$

From Fig. 5 we observe that  $\vec{e} - \vec{g}$  has the direction of  $\hat{k}^*$ , thus there exists  $\alpha$  such that  $\vec{e} - \vec{g} = \hat{a}\hat{k}^*$ . Using this into Eq. (32) the value of  $\alpha$  is found:

$$\alpha = (\vec{e} \cdot \hat{k} - D)(2\zeta^2)^{-1} \quad (34)$$

Finally, the obtained mapping from  $\vec{e}$  to  $\vec{g}$  is:

$$\vec{g}(\vec{e}) = \vec{e} - \hat{k}^*(\vec{e} \cdot \hat{k} - D)(2\zeta^2)^{-1} \quad (35)$$

#### 2.4. Summary of the procedure

The following list presents a summary of the steps to be performed for the application of the AIM method:

- For the three AIM variants presented, the first step is to fit a function to the measured TOFs. Using a polynomial function is a good choice because it is linear in its parameters and very fast implementations of linear least squares optimization exist. In the case of pulse-echo only one fitting is performed. In the pitch-catch case, fitting must be performed for each emitter, and in the plane wave case, for each emitted wave.
- The next step is to compute the partial derivatives of the fitted functions, which in the case of a polynomial is straight forward.
- A discrete set of aperture points must be defined to evaluate  $D(u, v)$  and its partial derivatives. A natural choice is to use the elements center points. This defines a  $N_u \times N_v$  rectangular grid, and evaluating the functions  $D(u, v)$ ,  $\frac{\partial D}{\partial u}(u, v)$  and  $\frac{\partial D}{\partial v}(u, v)$  in this grids results in three matrices.
- The corresponding equations of each method (Eqs. (7) for pulse-echo, (16) for pitch-catch and (35) for plane wave) are applied to those matrices. All the equations are composed of simple mathematical operations, except for the case of a plane wave with  $k_v \neq 0$ . In this exception, for each element in the grid, the roots of a non-linear one variable equation must be found by a numerical algorithm. Nevertheless, as explained in Section 2.3, the case  $k_v = 0$  is very useful, and it is solved by a closed formula.
- The final result is one entry point and the corresponding surface normal vector for each point in the aperture grid.

### 3. Experimental validation

For the validation of the methods presented in the previous sections, immersion testing experiments were performed with an aluminum test piece (Fig. 6). The ultrasound probe used is a 3 MHz,  $11 \times 11$  elements array by Imasonic (France). The array pitch is 1 mm resulting in a square aperture with 10 mm side length. The ultrasound equipment was a 128 channel full parallel SITAU by Dasel (Spain). The probe motion for the scanning procedure was done with 6-axis robotic arm by UR Robotics (Denmark). The test piece scanned region is shown in Fig. 6.a.

#### 3.1. Scan path design

The robotic arm was used to set the probe location and orientation in a WCS. This WCS is defined relative to the robot base. The test piece is placed inside the water tank, and its location and orientation in WCS are not known. Scan path planning for complex shapes like our test component is inherently difficult [15,16], especially when lacking a CAD model. We addressed this by using our surface detection method to interactively define a suitable scan path. First, the robotic arm is moved to place the probe in an initial  $PLO_0$  over the test piece, with a visual assessment ensuring approximate perpendicularity between the probe normal and the surface. The water height in  $PLO_0$  is chosen according to the maximum estimated depth to be acquired, in our case about 10 mm.

To design the scanning path, the robot controller is used to move the probe through a sequence of key PLOs:  $\{PLO_0, PLO_1, \dots, PLO_n\}$  (Fig. 7.a) These are chosen to roughly match the array face normal to the mean local surface normal and to keep an approximately constant probe standoff distance (the water height mentioned above). Then, the key PLOs are interpolated to generate intermediate PLOs, in such a way to cover the scanned region with the desired spatial sampling. The definition of spatial sampling in the case of complex probe path is not straightforward. While a simplified interpolation approach was used for this experiment, refining the sampling strategy within complex probe paths offers potential for future research.

The following simplified interpolation approach was adopted. Let  $PLO_i$  be defined in WCS by its 6 degrees of freedom as:

$$PLO_i = (x, y, z, \theta_x, \theta_y, \theta_z) \quad (36)$$

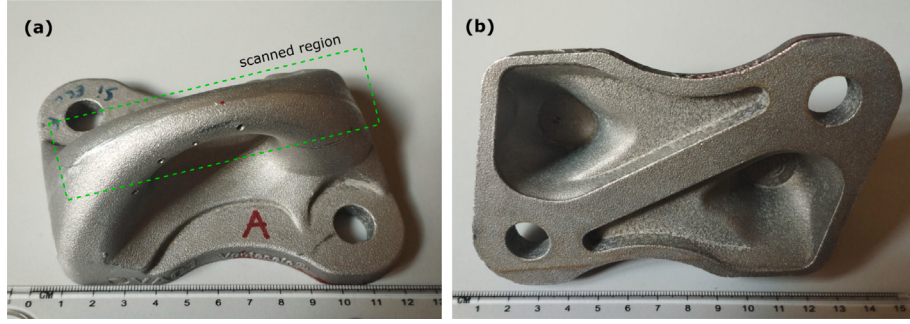


Fig. 6. Aluminum test piece used for the experimental validation. (a) Top view, (b) Bottom view.

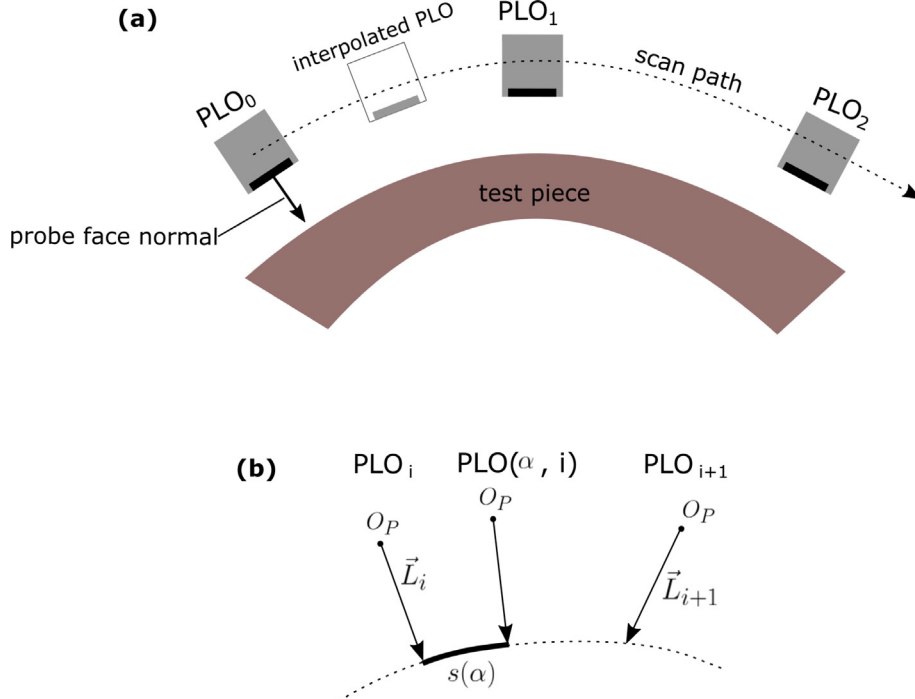


Fig. 7. Scan path design: (a) Schematic showing how the scan path is created by interpolation of key PLOs, (b) Detailed schematic for the mathematical implementation (Eq. (37)).

where  $(x, y, z)$  define the position and the orientation is given by the Euler angles  $(\theta_x, \theta_y, \theta_z)$ .

Between two consecutive key PLOs we use linear interpolation on each degree of freedom to define an intermediate PLO (Fig. 7.b) given by:

$$PLO(\alpha, i) = \alpha(PLO_{i+1} - PLO_i) + PLO_i \quad (37)$$

where  $0 < \alpha < 1$ .

An ordered set of  $M$  values,  $\{\alpha_{i,1}, \alpha_{i,2}, \alpha_{i,3}, \dots, \alpha_{i,M}\}$ , is chosen to define the  $M$  intermediate PLOs used for spatial sampling. To select those  $\alpha$  values we define, for each key PLO, a vector  $\vec{L}_i$  (Fig. 7.b), directed as the probe face normal. The length  $L = \|\vec{L}_i\|$  is a constant chosen to be approximately the water height. Thus, the tip of  $\vec{L}_i$  is approximately located on the component surface. For an intermediate PLO given by Eq. (37), there is a corresponding vector  $\vec{L}(\alpha, i)$ . As  $\alpha$  continuously changes from 0 to 1,  $\vec{L}(\alpha, i)$  tip describes a curve with arc length  $s(\alpha, i)$ . The scanning step is defined along that arc. If the desired step is  $\Delta s$ , then we compute  $M$  as:

$$M(i) = \text{round} \left( \frac{s(1, i)}{\Delta s} \right) \quad (38)$$

where  $s(1, i)$  is the total arc length between  $PLO_i$  and  $PLO_{i+1}$ . The  $\alpha$  values are set as:

$$\alpha(i, k) = \frac{k}{M(i)} \quad (39)$$

being  $k$  an integer in the interval  $[1, M(i)-1]$ . The equispaced  $\alpha$  values, generated by Eq. (39) in the interval  $[0, 1]$ , are assumed to map to equispaced points on the arc  $s(\alpha)$ , though this is an approximation.

In order to obtain about 50% array aperture overlap between two consecutive PLOs,  $\Delta s$  was set to 5 mm (half the square aperture side length). It is important to note, that aperture overlap can only be properly defined for planar scan path such that the aperture is on the path plane. This is not the case in our experiment. However, setting  $\Delta s = 5$  mm is a way to create a path such that the “shadow” of the aperture on the component surface has an approximate 50% overlap.

The final set of PLOs used for the scanning process is the union of the key PLOs and the intermediate interpolated PLOs. The total number of PLOs is then:

$$N_{PLO} = n + \sum_{i=0}^n M(i) \quad (40)$$

where  $n$  is the number of key PLOs.

For each of these  $N_{PLO}$  in the scanning path, a Full Matrix Capture (FMC) [9,17] acquisition is performed. Using the FMC matrix the three

presented methods were applied, as a plane wave acquisition can be synthesized from FMC data.

## 4. Results

### 4.1. Application and comparison of the three proposed methods

The first step is the measurement in each A-scan of the surface echo TOF. A thresholding method was used to detect the first high amplitude peak in the signal envelope, where the threshold value was manually tuned. This is a simple but not robust method, prone to outliers. In future works more robust and automatic methods for the detection of the surface echo must be researched, for example by the use of Neural Networks as in [18,19]. However, this is outside the scope of this work, in which we center our attention in the surface reconstruction once TOFs are known. The measured TOFs  $t_S^*(i, j)$  are a  $11 \times 11$  matrix. For the AIM method we need a continuous and differentiable function  $t_S(u, v)$  to compute the partial derivatives, or a method to estimate derivatives from a discrete sampling. The approach used was to fit a 2-degree polynomial function to the measured TOFs by least-squares. In order to minimize the effect of outliers, we used weighted fitting, where the weights were determined as in [12].

**Fig. 8** show results of the pulse-echo method for two different PLOs. **Fig. 8(a)** and **(b)** show the measured TOFs (A-scan sample index) along with the polynomial fitting. The color of points represents the weights. **Fig. 8(c)** and **(d)** show respectively the corresponding surface points computed, along with the array elements centers. Although the AIM method computes a continuous mapping from the array aperture to a surface patch, this function was evaluated in the array element centers in **Fig. 8(c)** and **(d)**. This sampling will be used later to fit another polynomial function to these points in order to get a local surface representation of the type  $w = f(u, v)$ , which will be used for computation of imaging focal laws.

Results for the three methods are compared in **Fig. 9**. For the pitch-catch method the result of only one emitter is shown (marked with the \* symbol in **Fig. 9**). For each emitter used, a different surface patch is reconstructed. In the case of the plane wave method, a single wave was used with direction vector  $(0, 0, -1)$ .

**Fig. 9** also shows the extension of the surface patch detected by each method. The pulse-echo methods detects the largest patch, followed by plane wave. Pitch-catch detects a significantly smaller patch, which is expected as the emission aperture used is a single element, while for the other two-methods the whole aperture is used. In order to reconstruct a greater surface path using the pitch-catch methods, more than one emitter should be used.

**Fig. 10** shows the resulting surface patches using the pitch-catch method for two different emitter sets. The emitters used are marked with \* symbol and a color, and the corresponding surface patch is rendered with the color of the associated emitter. It is observed that with less closely spaced emitters the surface patches cover a wider area, but leaving some “holes” (**Fig. 10.b**). Such “holes” are not a problem if the surface is sufficiently smooth, as in this case, because they may be filled by fitting function through the five patches.

An important fact to note in **Fig. 11** is the presence of some outliers: points which clearly deviate from the overall shape outlined by the set. This outliers are the effect of a problem in the function  $t_S(u, v)$ , shown inside the red ellipse in **Fig. 11.a**. This figure shows a B-scan type image depicting the received A-scans when the emitter was the  $(0,0)$  element (**Fig. 11.b**). The discontinuities observed in **Fig. 11.a** are the effect of an “unrolled” representation: array element linear index is row-wise in the  $u$  direction. Thus, A-scans from 0 to 10 correspond the first row, A-scans from 11, 21 correspond to the second row, etc. In **Fig. 11.a** the surface echo detected points are shown, along with the fitting function  $t_S(u, v)$  (black curve). It is observed that form some A-scans there is no detected first echo. The caused of this is that the threshold level was never crossed in those A-scans. A lower threshold would be

needed, but this might have an unwanted effect: the threshold being crossed by the probe surface wave signals which are present when using pitch-catch acquisition (**Fig. 11.a**). This type of problem in surface echo detection should be attacked with more advanced methods than simple thresholding.

In **Fig. 9** a comparison was done of the surface coverage each of the three methods achieves, but showing only one emitter for pitch-catch. What coverage can be achieved when using more emitters? To answer this question **Fig. 12** is presented, where the surface patches detected with the pulse-echo method and the pitch-catch with 5 emitters are compared for two different PLOs. The emitters used were  $[(0,0), (10, 10), (0, 10), (10, 0), (5, 5)]$  (central and corner elements). It can be observed that the 5 pitch-catch patches cover almost the same area as the pulse-echo patch. This is an important result, because it shows that in some cases, using 5 shots (pitch-catch) instead 121 (pulse-echo) the same surface coverage might be achieved. Therefore, almost the same result could be obtained with 24 times faster acquisition. Nevertheless, in an application were FMC is used, all elements need to be fired for imaging, and thus, the pulse-echo method would be the best choice. In other applications, like Phased Array or plane wave imaging, two different acquisition steps are used: first a surface detection step, and then, imaging acquisition. In that kind of scenarios the pitch-catch method will be useful to obtain a faster image rate, reducing the time required for the surface detection acquisition.

### 4.2. Global surface reconstruction

The results presented in the previous sections were local surface patches corresponding to individual PLOs. The scan of the test piece consisted of 24 PLOs along the scan path. In order to get a global surface patch over all the scanned region, the local patches must be merged. Each patch is the set of points that results from the evaluation of the mapping on a discrete set of array aperture points. As in the previous section, the aperture points selected were the array elements centers, which is the more natural choice. The surface points in each patch are represented by its PCS coordinates. For the global patch, they must be rotated and translated according to the corresponding PLO using the data provided by the robot software. After this operation we have the WCS coordinates of all the patches. The global patch obtained with the pulse-echo method is shown, as example, in **Fig. 13**, where it is also plotted over a 3D model of the test piece obtained by 3D laser scanning (Artec Space Spider by Artec3D (Luxembourg))

### 4.3. Measurement error analysis

In order to estimate the measurement errors in the surface points detected, a reference is needed. We used as reference the 3D model (cloud of points) shown in **Fig. 13**, obtained by laser scanning, with a precision of  $0.05 \text{ mm} + 0.3 \text{ mm/m}$  according to the instrument manufacturer. The model was scanned with distances about  $0.3 \text{ m}$ , thus the estimated error is  $0.06 \text{ mm}$ .

For the purpose of comparing the reference model with the ultrasonically measured surface patch, a 3D registration process [20] is needed to locate the two point sets in the same reference system. We applied the Iterative Closest Point (ICP) method [21]. The ICP method is based on the minimization of the distances between to point sets (or point clouds). Given a target point cloud  $A$  and a source point cloud  $B$ , first an initial transformation  $T_0$  is found, which roughly matches the two sets. Then for each point  $a$  in  $A$ , the closest point  $b$  in  $B$  is found. The set  $\Lambda_0 = (a, b)$  is called the correspondence set. The ICP algorithm iterates over two steps:

1. Given the current correspondence set, find an updated transformation  $T_i$  by minimizing the cost function  $E(T_i) = \sum_{(a,b) \in \Lambda_i} \|b - T_i(a)\|$ .
2. Compute the updated correspondence set.

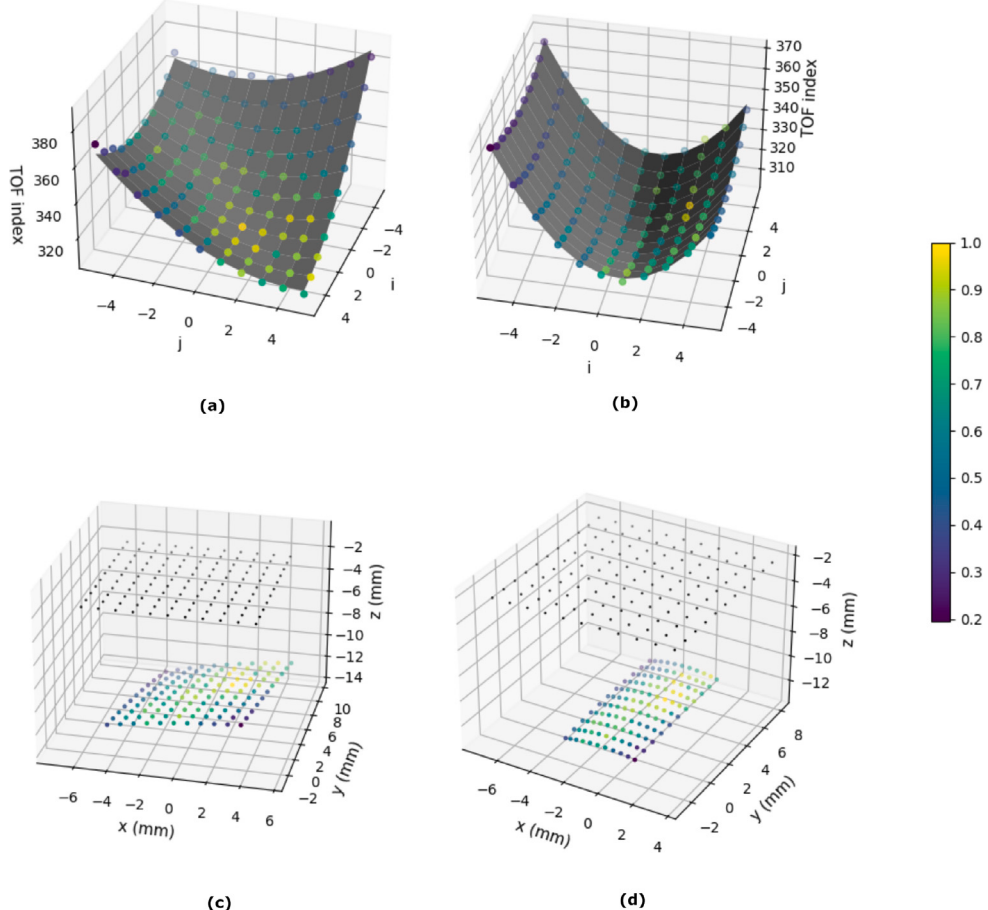


**Fig. 8.** Pulse-echo method results for two different PLOs. (a) and (b) TOF index fitting. (c) and (d) Computed surface points and array element centers (black dots). (For interpretation of the references to color in this figure legend, the reader is referred to the web version of this article.)

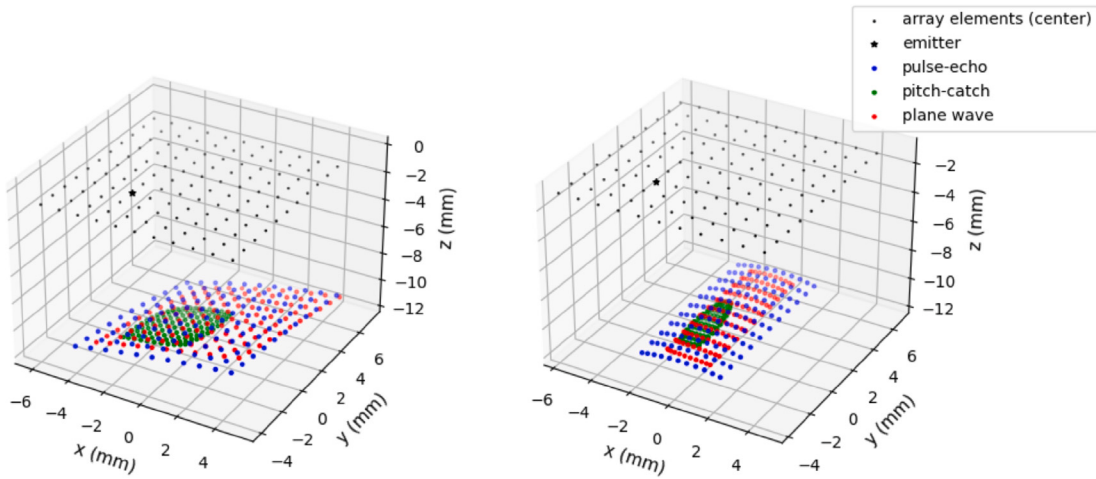


**Fig. 9.** Results of the three methods for two different PLOs.

The ICP algorithm was applied with the Open3D open-source library [22]. Using the resulting correspondence set the difference between each ultrasonically measured point and the corresponding one in the reference model is computed. This is used as a measure of the error. Error statistics for the three methods are presented in Table 1. Fig. 14 shows the error distribution in the pulse-echo method. The distributions for the other two methods are quite similar and are not shown for the sake of brevity.

The results presented in Table 1 show that for the three methods the error means are significantly small, in the order of a few micrometers (for the three coordinates). It is important to note that these values are subjected to bias resulting from the ICP registration. As ICP works by minimizing the distances between points, it can match the surfaces better than they really match. To avoid this problem it would be necessary to measure the 3D scan point cloud and the ultrasound point cloud in the same coordinate system, in order to get a direct comparison. The implementation of such a measurement requires a

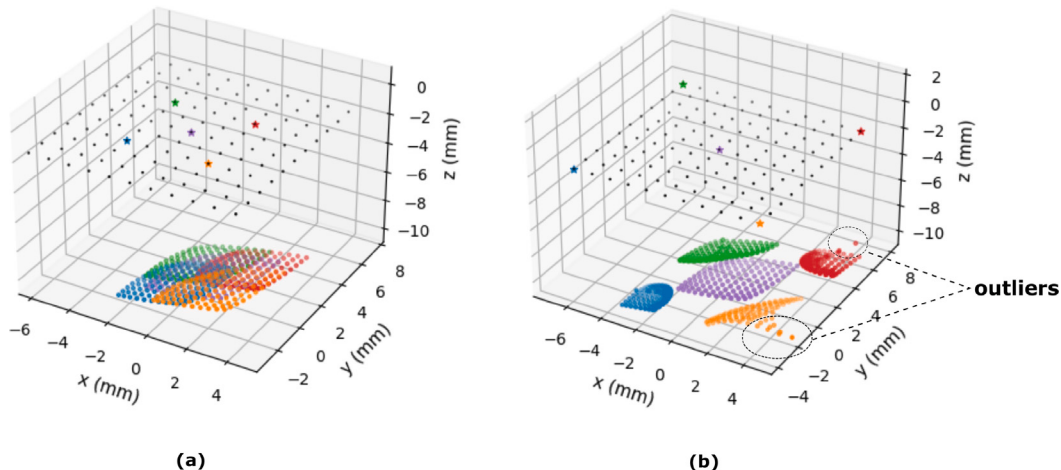


**Fig. 10.** Surface patches detected with different 5 emitter groups using the pitch-catch method. Emitters (i, j) indexes: (a) [(2,2), (7, 2), (2, 7), (7, 7), (5, 5)], (b) [(0,0), (10, 10), (0, 10), (10, 0), (5, 5)]. (For interpretation of the references to color in this figure legend, the reader is referred to the web version of this article.)

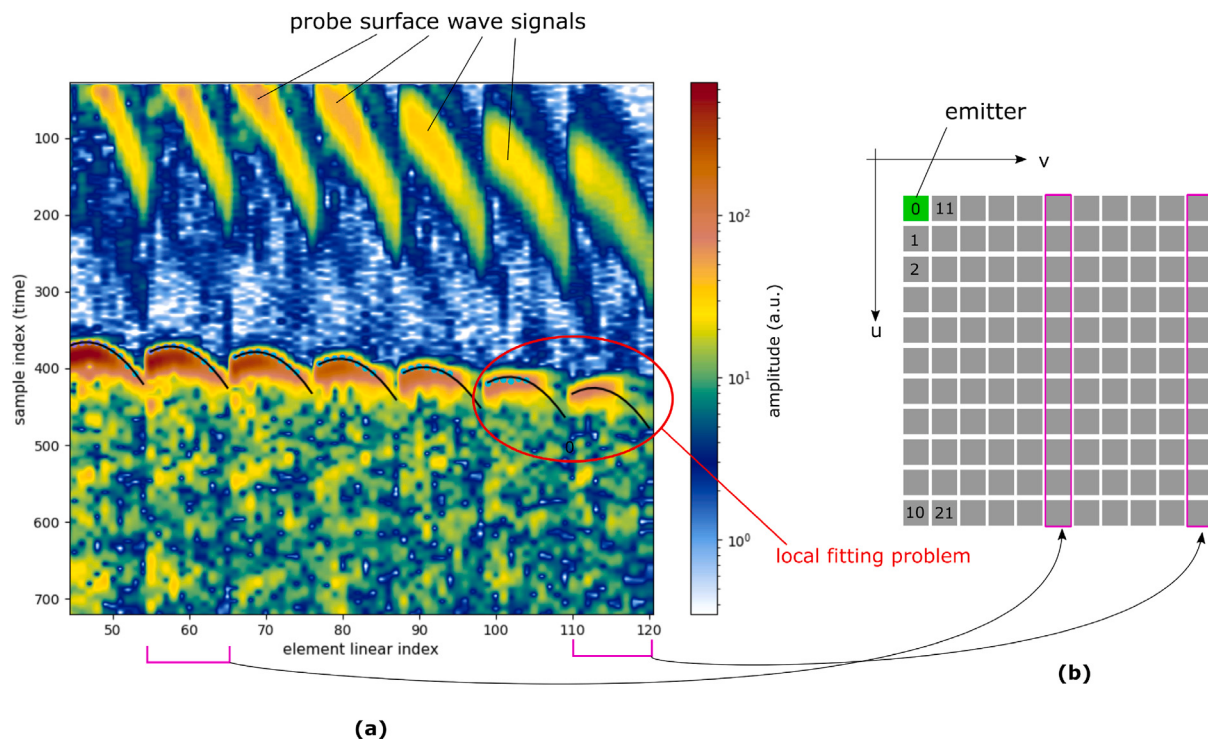


**Fig. 11.** TOF fitting problem that causes outliers in surface reconstruction. (a) A-scans measured when emitting with element (0, 0). The dots indicate where the amplitude threshold is crossed and the black curves the TOF fitting function. (b) Array elements, where the linear indexes of some elements are shown. The emitter (green), has 2D indexes (0,0) and linear index 0. (For interpretation of the references to color in this figure legend, the reader is referred to the web version of this article.)

complex and finely calibrated set-up where the relative position and orientation of the ultrasound probe and the 3D scanner are precisely measured. Nevertheless, the standard deviation of errors can be used as a quite realistic estimation of the measurement error, as they represent the relative errors along the part, which would affect image quality through focusing errors. The standard deviation values are in the order of 0.1 mm [1] for the three methods.

#### 4.4. TFM imaging with the measured surface

In this section, we used the reconstructed surface to compute TFM images of the test piece. For each PLO in the scan path, the AIM mapping is evaluated on the array elements centers, resulting in a discretized local surface patch that we fit with a function  $w = f(u, v)$ .

**Table 1**  
Error(in micrometers) statistics for (x,y,z) coordinates for the three presented methods computed by the ICP registration.

	Pulse-echo			Pitch-catch			Plane wave		
	mean	std	max	mean	std	max	mean	std	max
x (μm)	0.8	120	480	1.1	70	250	-2.3	80	250
y (μm)	0.4	110	380	1.3	70	280	6.6	80	340
z (μm)	4.3	180	650	-0.5	100	330	-1.8	120	460

This function, which locally models the surface, is used to compute TOFs using Fermat's principle [11]. Second degree polynomials were used for the fitting, as they resulted adequate to the smooth curvature of the test piece.

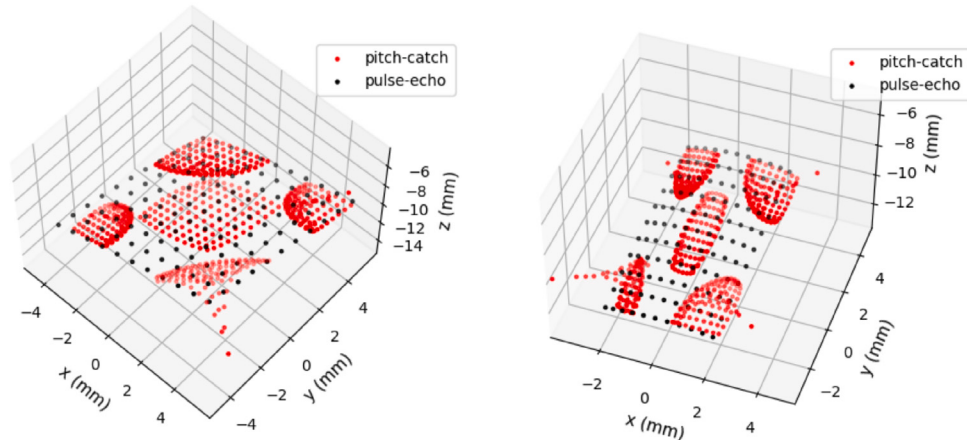


Fig. 12. Comparison of the surface coverage resulted from pulse-echo and the 5 emitter pitch-catch method.

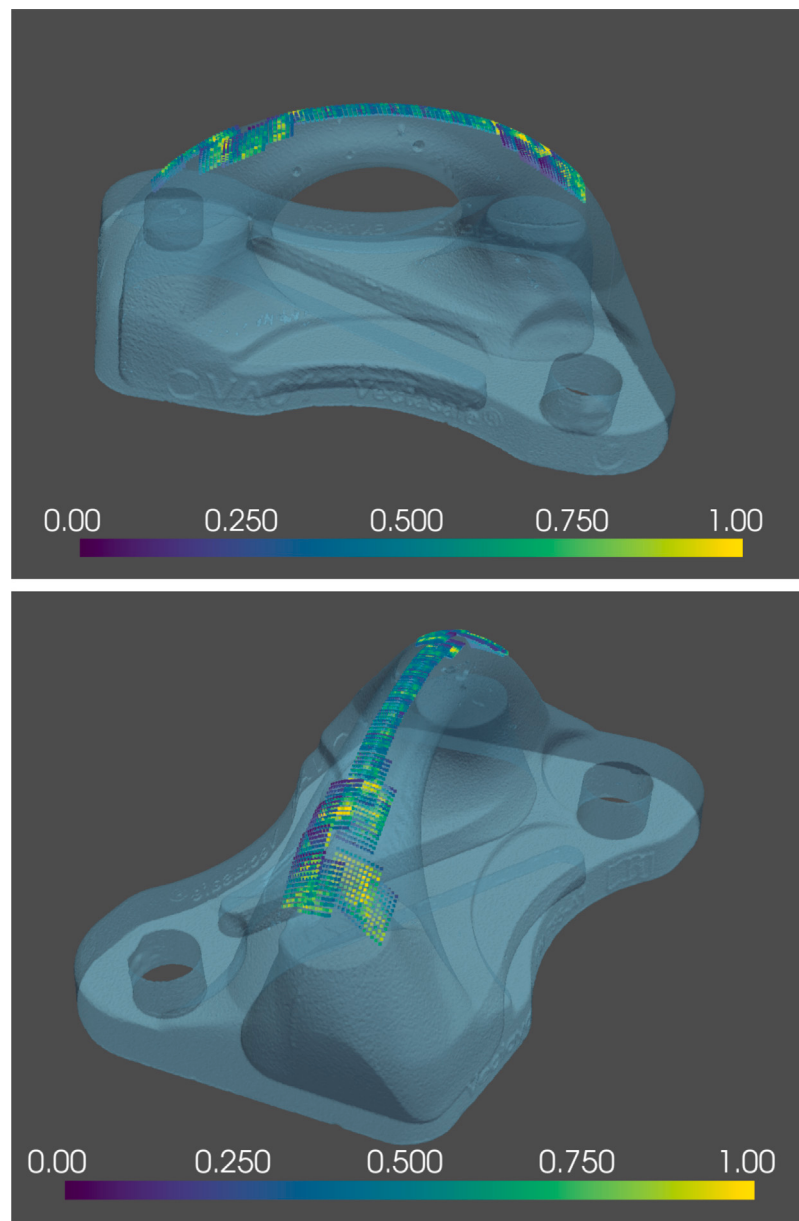


Fig. 13. Global surface patch reconstructed by pulse-echo method and 3D model obtained by 3D laser scanning.

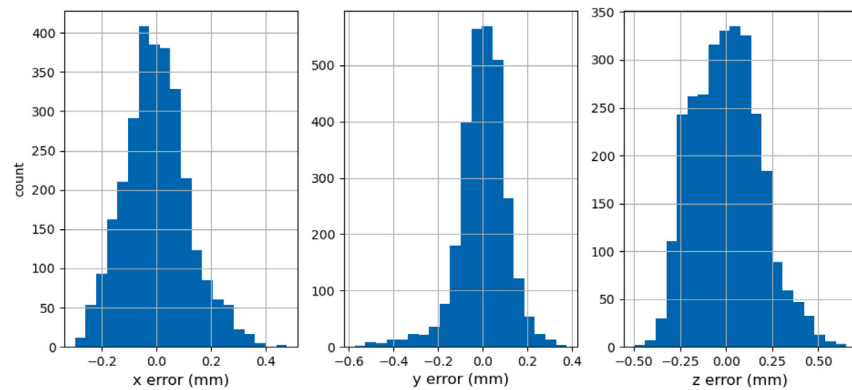


Fig. 14. Measurement error histograms for the 3 space coordinates.

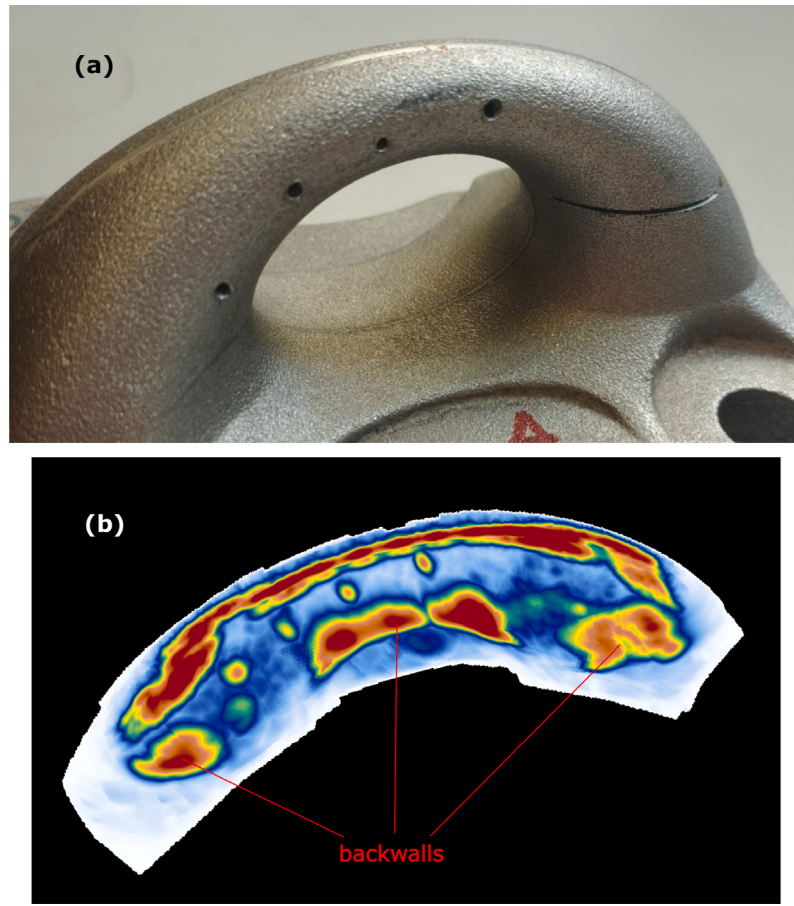


Fig. 15. 3D TFM image of the test piece scanned region. (a) Photograph with similar viewing angle (b) TFM image.

A local TFM image was computed in the PCS for each PLO. Then all the 24 images were stitched together. For that purpose, each image must be transformed to the WCS by a process of translation, rotation and trilinear interpolation. The resulting global volumetric image is shown in Fig. 15.b, along with photograph (15.a) of the test piece from a similar viewing angle.

The test piece has a set of artificial defects used to test the imaging performance. In Fig. 15.a four side drilled holes can be seen. It is observed in 15.b that the four holes were clearly imaged. Additionally, we can observe the backwall in the curved zone, and in the two planar parts (which can be observed in the photograph in Fig. 6.b). Fig. 15.a also shows a notch defect that cannot be observed in the TFM image. This is caused by the 3D view which hides certain image features. To observe the notch indication we use the D-scan image in Fig. 17.b.

As unexpected indications were observed in the TFM images, X-ray micro tomography (micro-CT) was applied to the test piece. Figs. 16.a and 17.a show two micro-CT slices, where the presence of porosity is revealed. Fig. 16.a also shows the other artificial defects created in the test piece: 2 bottom drilled holes from the planar zones. The one in the right got merged into a pore cluster, creating a big zone of high amplitude indications (Fig. 16.b) where the hole indication cannot be discriminated. On the other hand, the tip indication of the other bottom-drilled hole can be appreciated in the left side of Fig. 16.b.

#### 4.5. Discussion

It was shown for the test piece that the three proposed surface reconstruction methods performed well, with an estimated error of 0.1 mm.

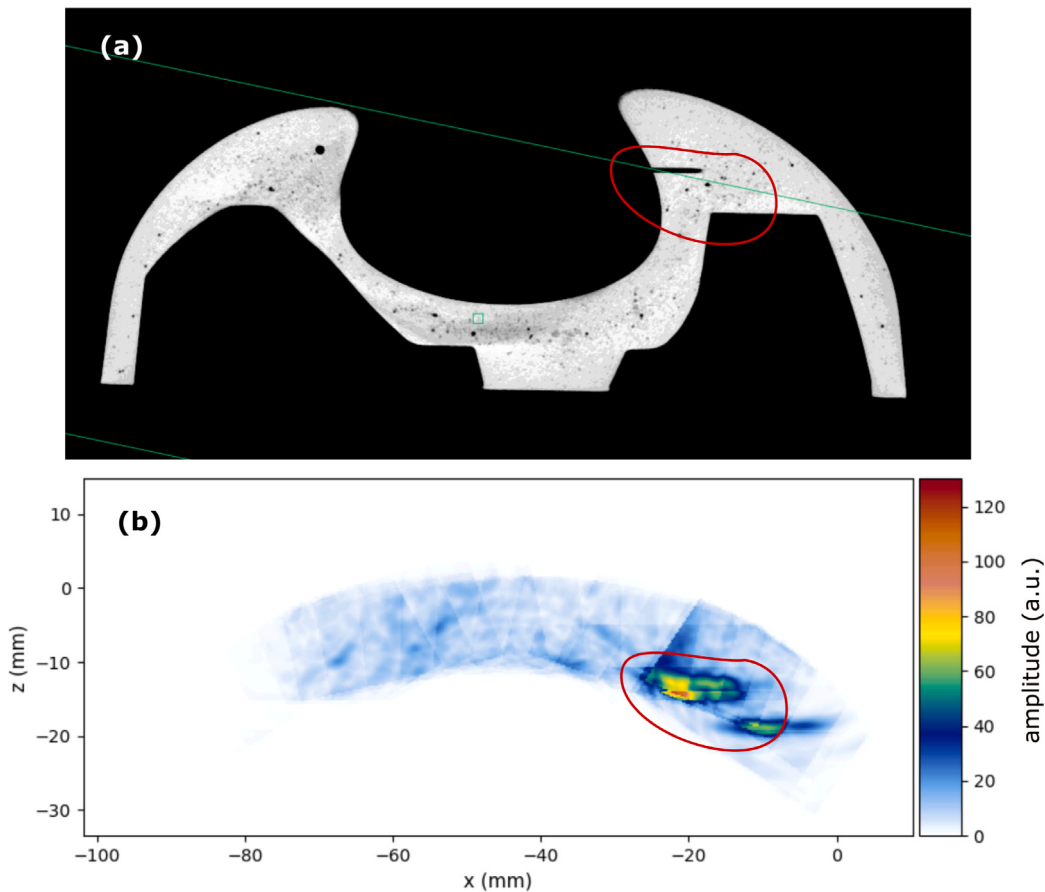


**Fig. 16.** Comparison of TFM D-scan and micro CT slice where the groove defect can be appreciated. (a) Micro CT slice (b) TFM D-scan.

The pulse-echo method, which requires the firing of all elements (121 shots) achieved a similar surface coverage than the pitch-catch method with five shots. Nevertheless, the pitch-catch option produces a surface patch with some “holes”. This effect might be problematic if the local surface patch has a more complex shape. As an example, Fig. 18 shows a 2D case where using only three elements will not capture all the surface features. If such a problem is expected, more emitters should be used. With respect to the plane-wave method, it resulted in a smaller detected patch than pulse-echo and 5 emitter pitch-catch methods, but it used only one shot, thus being the one with faster acquisition. The plane wave methods can be applied with more shots, using waves in other directions, which could detect other surface patches and thus increase the overall coverage. Nevertheless, the other directions should be chosen in a rather arbitrary fashion unless the user has some prior knowledge on surface orientation relative to the probe. Additionally, using plane waves in directions different to  $(-1, 0, 0)$  requires more computations, as a numerical root-finding algorithm must be applied for Eq. (26).

The error distributions shown in Fig. 14 have very small mean values, less than 10 micrometers. These values are expected to be underestimated as an effect of the ICP registration algorithm applied to compare the measurements with the reference surface model. Larger systematic errors should be expected, specially in the w-direction, as discussed in [12]. Nevertheless, as the ultrasonically measured surface is not just a rigid transformation of the real surface, there are also some shape differences that are not removed by ICP. These differences, along with random noise, are the source of variance in the error distributions, with a standard deviation in the order of 0.1 mm for the three methods, in the three spatial directions.

## 5. Conclusions

The AIM method was presented to map the TOFs from probe aperture points to the test piece surface points. The method has three variants depending on the type of acquisition used: pulse-echo, pitch-catch or plane wave. It was shown that for the studied test piece the three variants can detect and reconstruct a local surface patch with a 0.1 mm estimated error, although an additional systematic error of the same order of magnitude is expected in the w-direction (probe face normal), as discussed in [12].

The surface extent covered by the three methods was compared, showing in the presented example that the pulse-echo method and pitch-catch with 5 emitters reconstruct a similar surface patch, but in the pitch-catch case the sparsity of the emitting aperture leaves some undetected spots or “holes”. In contrast, the plane wave method using a single wave directed as  $(-1, 0, 0)$  resulted in a smaller surface patch, but with the benefit of faster acquisition.

An experimental example was shown where the AIM method is used for TFM 3D imaging of a complex test component scanned using a 6-axis robotic arm. The scanning procedure was performed without knowledge of the test component location and orientation relative to the robot coordinate system. Instead, the scan path was constructed by an empirical method where the user selects a set of key PLOs and then the probe path is computed to interpolate these PLOs. This procedure simplifies the testing process by removing the requirement for a CAD model. It measures the component's surface directly during scanning. Additionally, it tolerates variations in component positioning, as the surface reconstruction method can account for minor offsets. These features demonstrate the method's strong potential for industrial applications.

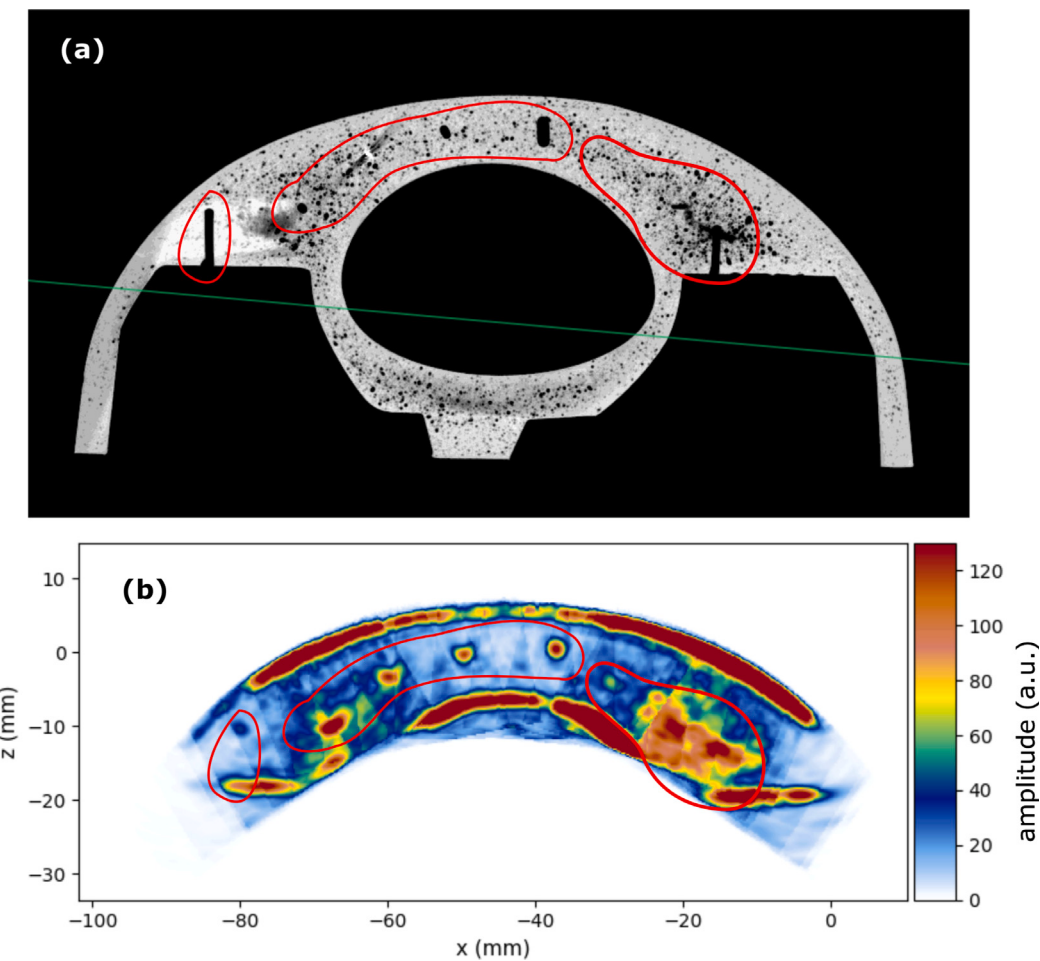


**Fig. 17.** Comparison of TFM D-scan and micro CT slice where the side drilled holes, the bottom drilled holes and a porosity cluster are shown. (a) Micro CT slice (b) TFM D-scan.

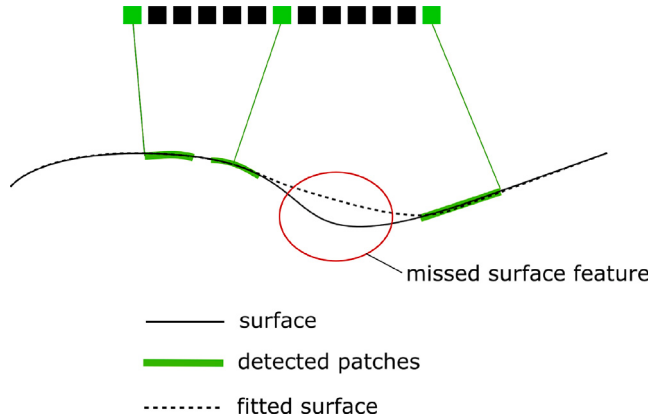


**Fig. 18.** Schematic showing the “hole” problem that could arise when using the pitch-catch method with a small number of emitters.

#### CRediT authorship contribution statement

**Guillermo Cosarinsky:** Writing – original draft, Validation, Software, Methodology, Formal analysis, Conceptualization. **Jorge F. Cruza:** Writing – review & editing, Supervision, Conceptualization. **Mario Muñoz:** Writing – review & editing, Software. **Adrián Rubio:** Writing – review & editing, Software. **Jorge Camacho:**

Writing – review & editing, Validation, Supervision, Methodology, Conceptualization.

#### Declaration of competing interest

The authors declare that they have no known competing financial interests or personal relationships that could have appeared to influence the work reported in this paper.

#### Acknowledgments

This research was supported by the project PID2022-143271OB-I00, funded by MCIN/AEI /10.13039/501100011033/FEDER, UE, the project PLEC2024-011165, funded by MICIU/AEI/10.13039/501100011033/ FEDER, UE , and by the European Commission – NextGenerationEU, through Momentum CSIC Programme: Develop Your Digital Talent. The funding for these actions/grants and contracts comes from the European Union’s Recovery and Resilience Facility-Next Generation, in the framework of the General Invitation of the Spanish Government’s public business entity Red.es to participate in talent attraction and retention programmes within Investment 4 of Component 19 of the Recovery, Transformation and Resilience Plan.

G. Cosarinsky staff is hired under the Generation D initiative, promoted by Red.es, an organization attached to the Ministry for Digital Transformation and the Civil Service, for the attraction and retention of talent through grants and training contracts, financed by the Recovery, Transformation and Resilience Plan through the European Union’s Next Generation funds

## Data availability

Data will be made available on request.

## References

- [1] Waltham DA. Two-point ray tracing using Fermat's principle. *Geophys J Int* 1988;93(3):575–82. <http://dx.doi.org/10.1111/j.1365-246X.1988.tb03883.x>, ISSN:0956-540X.
- [2] Robert S, Calmon P, Calvo M, Le Jeune L, Iakovleva E. Surface estimation methods with phased-arrays for adaptive ultrasonic imaging in complex components. *AIP Conf Proc* 2015;1650(2015):1657–66. <http://dx.doi.org/10.1063/1.4914787>.
- [3] Drinkwater Bruce W, Wilcox Paul D. Ultrasonic arrays for non-destructive evaluation: A review. *NDT E Int* 2006;39(7):525–41. <http://dx.doi.org/10.1016/j.ndteint.2006.03.006>, ISSN: 09638695.
- [4] Schmerr Lester W. Fundamentals of ultrasonic phased arrays. In: *Solid mechanics and its applications*. Vol. 215, 2015, ISBN: 9783319072715.
- [5] Sutcliffe M, Weston M, Charlton P, Donne K, Wright B, Cooper I. Full matrix capture with time-efficient auto-focusing of unknown geometry through dual-layered media. *Insight Non-Destr Test Cond Monit* 2013;55(6):297–301. <http://dx.doi.org/10.1784/insi.2012.55.6.297>.
- [6] Matuda MY, Buiochi F, Adamowski JC. Experimental analysis of surface detection methods for two-medium imaging with a linear ultrasonic array. *Ultrasonics* 2019;94(August 2018):50–9, URL: <https://doi.org/10.1016/j.ultras.2018.12.004>, ISSN:0041624X.
- [7] Chen Qiping, Xie Yinfai, Cao Huanqing, He Zike, Wang Dawei, Guo Shifeng. Ultrasonic inspection of curved structures with a hemispherical-omnidirectional ultrasonic probe via linear scan SAFT imaging. *NDT E Int* 2022;129(February):102650, URL: <https://doi.org/10.1016/j.ndteint.2022.102650>, ISSN: 09638695.
- [8] Camacho J, Cruza FJ, Brizuela J, Fritsch C. Automatic dynamic depth focusing for NDT. *IEEE Trans Ultrason Ferroelectr Freq Control* 2014;61:673–84.
- [9] Holmes Caroline, Drinkwater Bruce, Wilcox Paul. The post-processing of ultrasonic array data using the total focusing method. *Insight: Non-Destr Test Cond Monit* 2004;46(11):677–80. <http://dx.doi.org/10.1784/insi.46.11.677.52285>, ISSN: 13542575.
- [10] McKee JG, Bevan RLT, Wilcox PD, Malkin RE. Volumetric imaging through a doubly-curved surface using a 2D phased array. *NDT E Int* 2020;113(August):102260. <http://dx.doi.org/10.1016/j.ndteint.2020.102260>.
- [11] Cosarinsky G, Cruza JF, Muñoz M, Camacho J. Optimized auto-focusing method for 3D ultrasound imaging in NDT. *NDT E Int* 2023;134(November 2022). <http://dx.doi.org/10.1016/j.ndteint.2022.102779>, ISSN: 09638695.
- [12] Cosarinsky G, Cruza JF, Muñoz M, Camacho J. Automatic estimation of surface and probe location for 3D imaging with bidimensional arrays. *NDT E Int* 2024;141:102990. <http://dx.doi.org/10.1016/j.ndteint.2023.102990>, URL: <https://www.sciencedirect.com/science/article/pii/S0963869523002050>, ISSN: 0963-8695.
- [13] Sakamoto Takuya, Sato Toru. A target shape estimation algorithm for pulse radar systems based on boundary scattering transform. *IEICE Trans Commun* 2004;E87-B:1357–65, ISSN: 09168516.
- [14] Sakamoto Takuya. A fast algorithm for 3-dimensional imaging with UWB pulse radar systems. *IEICE Trans Commun* 2007;E90-B:636–44. <http://dx.doi.org/10.1093/ietcom/e90-b.3.636>, ISSN: 17451345.
- [15] Zhang Yang, Chen Kai, Guo Peng, Li Fan, Zhu Jiang, Zhu Li-Min. Profile tracking for multi-axis ultrasonic inspection of model-unknown free-form surfaces based on energy concentration. *Measurement* 2021;172:108867. <http://dx.doi.org/10.1016/j.measurement.2020.108867>, URL: <https://www.sciencedirect.com/science/article/pii/S0263224120313579>, ISSN: 0263-2241.
- [16] Morozov M, Pierce SG, MacLeod CN, Mineo C, Summan R. Off-line scan path planning for robotic NDT. *Measurement* 2018;122:284–90. <http://dx.doi.org/10.1016/j.measurement.2018.02.020>, URL: <https://www.sciencedirect.com/science/article/pii/S0263224118301131>, ISSN: 0263-2241.
- [17] Holmes Caroline, Drinkwater Bruce W, Wilcox Paul D. Post-processing of the full matrix of ultrasonic transmit-receive array data for non-destructive evaluation. *NDT E Int* 2005;38(8):701–11. <http://dx.doi.org/10.1016/j.ndteint.2005.04.002>, ISSN: 09638695.
- [18] Qu Xiaolei, Yan Guo, Zheng Dezhi, Fan Shangchun, Rao Qiyu, Jiang Jue. A deep learning-based automatic first-arrival picking method for ultrasound sound-speed tomography. *IEEE Trans Ultrason Ferroelectr Freq Control* 2021;68(8):2675–86. <http://dx.doi.org/10.1109/TUFFC.2021.3074983>, ISSN: 15258955.
- [19] Guo Xiaolong. First-arrival picking for microseismic monitoring based on deep learning. *Int J Geophys* 2021;2021. <http://dx.doi.org/10.1155/2021/5548346>, ISSN: 16878868.
- [20] Pomerleau François, Colas Francis, Siegwart Roland. A review of point cloud registration algorithms for mobile robotics. *Found Trends® Robot* 2015;4(1):1–104, URL: <http://dx.doi.org/10.1561/2300000035>, ISSN: 1935-8253.
- [21] Besl PJ, McKay ND. A method for registration of 3-D shapes. *IEEE T. Pattern Anal.* 1992;14:239–56.
- [22] Zhou Qian-Yi, Park Jaesik, Koltun Vladlen. Open3D: A modern library for 3D data processing. 2018, [arXiv:1801.09847](https://arxiv.org/abs/1801.09847).